Reappraisal of gravity instability conditions for offshore wedges: consequences for fluid overpressures in the Niger Delta

Bertrand Maillot, Y. Leroy, Xiaoping Yuan

Geophysical Journal International

Geophys. J. Int. (2017) **208,** 1655–1671
Advance Access publication 2016 December 17
GJI Geodynamics and tectonics

doi: 10.1093/gji/ggw474

Reappraisal of gravity instability conditions for offshore wedges: consequences for fluid overpressures in the Niger Delta

X.P. Yuan,[1,*] Y.M. Leroy[1,†] and B. Maillot[2]

[1] *Laboratoire de Géologie, CNRS, École Normale Supérieure, F-75005 Paris, France. E-mail: xyuan@geologie.ens.fr*
[2] *Laboratoire de Géosciences et Environment, Université de Cergy-Pontoise, F-95011 Cergy-Pontoise, France*

Accepted 2016 December 16. Received 2016 December 7; in original form 2016 August 7

SUMMARY

Gravity instabilities in offshore deltas often involve three structural domains in interaction by the weak detachment plane: an upslope extensional region, a transitional domain sliding seaward, and a downslope compressive region. We provide the fluid pressure conditions for the gravity instabilities due to the interaction of these three structural domains. For that purpose, we apply the kinematic approach of Limit Analysis which relies on the mechanical equilibrium and on the assumption that the onset of the instability is indeed triggered by the motion of the three domains if the Coulomb criterion is met on all slipping faults. The Limit Analysis predictions include the detachment activation length and the normal and thrust fault dips for any given topographic profile. The approach is validated by showing that our predictions match the experimental results on normal faulting triggered by air overpressure in sand analogues. For offshore wedges, the stabilizing effect of the frontal thrusting and of the transitional zone sliding requires large overpressures to reduce friction within the detachment and upslope sediment deposition to trigger the instability. As a consequence, the topographic slope is found to be several degrees larger than predicted with the Critical Coulomb Wedge (CCW) theory which does not account for the interaction of the three domains. The difference in predictions between the two theoretical approaches is important for length ratio less than 100, defined by the ratio of the detachment activated length to the downslope sediment thickness. Fitting our prototype to the offshore Niger Delta and estimating the above length ratio to be in the range of 30–70, it is found that, for cohesionless materials, the effective friction coefficient μ'_B is less than 0.27 within the bulk material and μ'_D is less than 0.017 in the detachment for the gravity instability to occur. These values are lower than those previously determined ($\mu'_B = 0.5-0.9$, $\mu'_D = 0. - 0.2$) by considering only the compressive domain and applying the CCW theory. These new values correspond to a pore-fluid pressure in the range of 80–90 per cent of the lithostatic pressure within the bulk material (Hubbert–Rubey fluid-pressure ratio 0.8–0.9), and in the range of 97–99 per cent of the lithostatic pressure within the detachment.

Key words: Geomechanics; Sedimentary basin processes; Dynamics and mechanics of faulting; Dynamics: gravity and tectonics; Mechanics, theory, and modeling; Africa.

1 INTRODUCTION

Regional seismic studies across the Amazon Fan (Silva *et al.* 1998; Cobbold *et al.* 2004), the offshore Niger Delta (Weber & Daukoru 1975; Hooper *et al.* 2002; Maloney *et al.* 2010), and the offshore Brunei wedge (Tingay *et al.* 2009; King *et al.* 2010) show normal faulting in the thick, coastal part on the shelf and simultaneous thrusting in the thin, deep part, with all faults rooted on a common detachment level. These structures are thus typically characterized by three successive domains above the weak detachment: the upslope extensional province, the transitional sliding domain, and the downslope compressive province. They are interpreted as the result of gravity-driven mechanical instabilities triggered by the sediment loading and the associated high fluid pressures at depth (Damuth 1994). Our objective is to propose a 2-D methodology to capture the fluid pressure conditions at the onset of these gravity instabilities, accounting for the interaction of the three

* Now at: Helmholtz Centre Potsdam, German Research Center for Geosciences (GFZ), F-14473 Potsdam, Germany.
† Now at: Total SA, CSTJF, F-64000 Pau, France.

structural provinces. This methodology relies on an assumption, shared with the classical Critical Coulomb Wedge (CCW) theory, that the detachment, composed of shales, is frictional and cohesive.

The link between extensional and compressive provinces during gravity instability was demonstrated experimentally. The wedge prototype composed of a progradational dry sand on a viscous silicone substratum considered by Ge *et al.* (1997); McClay *et al.* (1998); Rowan *et al.* (2004); Vendeville (2005) results in the synchronous development of an upslope graben system and a downslope fold-and-thrust belt. These experiments however do not capture the influence of the fluid overpressures. It is only recently that analogue experiments with air flow through sand have been proposed (Mourgues & Cobbold 2003, 2006b) to simulate the onset and the evolution of overpressured, gravity-driven shale deltas.

The interaction between the three structural provinces was also questioned on theoretical grounds. Crans *et al.* (1980) proposed an exact, analytical solution based on the slip line theory to capture listric faults for frictional, overpressured materials considering an inclined layer. Their approach applies to the extensional and compressive domains. The difference in forces parallel to the slope in these two regions is then balanced assuming a frictional detachment providing the extent of the intermediate region. The main difference with the CCW theory of Dahlen (1984) is that the latter approach applies to a wedge. The CCW theory generalized the concept of slope instability well known in civil engineering to the length scale of sedimentary, saturated wedges. It applies to the extensional upslope (active) and to the compressive downslope (passive) domains but does not propose any connection between the two. The extent of the intermediate region can also be estimated following the same argument of Crans *et al.* (1980), for an inclined layer, as presented by Mourgues *et al.* (2009).

There has been some applications of the CCW theory to fluid-saturated wedges (Bilotti & Shaw 2005; Suppe 2007, 2014) on the Niger Delta frontal compressive region, assuming a frictional behaviour of the sediments and the detachment. It was found that the pore-fluid pressure within the detachment is 90 per cent of the lithostatic pressure (Hubbert-Rubey fluid-pressure ratio $\lambda \sim 0.9$).

Our objective is to continue this line of work on the Niger Delta and to propose a methodology for capturing the interaction between the three domains of the collapsing wedges assuming complex geometry and cohesive materials. It is a 2-D analytical application of the kinematic approach of Limit Analysis (Chen 1975; Salençon 2002) as presented by Maillot & Leroy (2006) for dry frictional materials and by Pons & Leroy (2012) and Yuan *et al.* (2015), referred to as paper 1 in what follows, for fluid-saturated media. The application of Limit Analysis to the offshore Niger Delta allows us to re-evaluate the fluid pressures to even larger levels than those already inferred by Bilotti & Shaw (2005), confirming the earlier predictions of Albertz *et al.* (2010).

This contribution contents are as follows. Section 2 and Appendix A concern the presentation of the Limit Analysis for the gravity instability with three structural domains. Section 3 validates this method by comparing the predictions with analytical (Hubbert & Rubey 1959; Lacoste *et al.* 2012) and experimental (Mourgues & Cobbold 2006a) estimations of the collapse length and fault dips for an inclined layer. This methodology is then applied to the offshore Niger Delta to constrain the fluid pressures necessary to produce the current activation of the three structural domains. The Supporting Information proposes a comparison of the various fluid overpressure parametrizations found in the literature as well as the complete derivation of the solution of Lacoste *et al.* (2012), for the sake of completeness.

2 GRAVITY INSTABILITIES WITH LIMIT ANALYSIS

The concept of gravity instability discussed above is now developed into a prototype amenable to theoretical analysis, with an extensional upslope (active) and a compressive downslope (passive) domain. The Limit Analysis is then presented for the general case of a wedge with an arbitrary topographic profile and fluid overpressures.

2.1 General prototype

The geometry of our prototype and the gravity-driven collapse mechanism are presented in Fig. 1. The domain is composed of a uniform, fluid saturated material and has an irregular topography. It rests on a planar detachment (*AB*) inclined at the angle β (positive if dipping

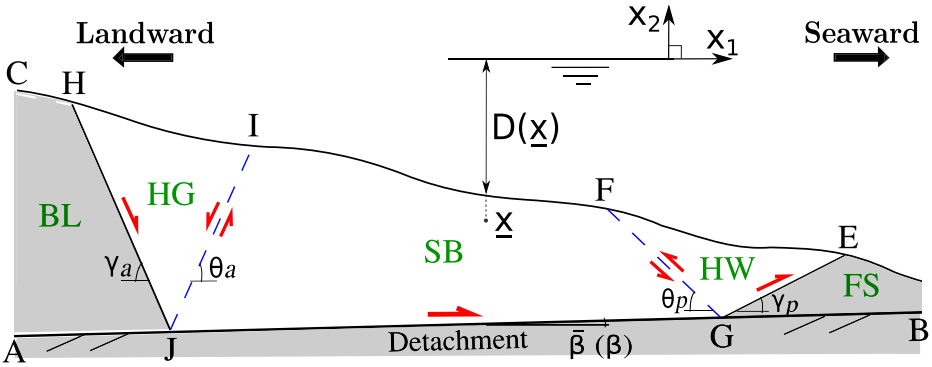

Figure 1. The general prototype and the collapse mechanism for gravitational instabilities. The half-graben (HG) collapse drives the sliding of the transitional region (sliding block SB) up to the thrusting at point *G* with the hanging wall (HW) (semi-arrows along the faults *JH*, *GE* and the active detachment *JG* and double semi-arrows across the axial surfaces *JI* and *GF*).

landward, and $\bar{\beta}$ denotes the absolute value of β). The bulk material and the detachment are frictional with distinct cohesions C_i and friction angles φ_i, with the subscript i set to B or D, respectively. The same notation is used through this work for cohesions and friction angles and only the subscript i will be defined for new domains or faults in what follows. The gravity instability results from the normal fault *JH* and the thrust ramp *GE*, simultaneously active with the sliding on the detachment *JG*. These faults could have different properties from the bulk material and the subscripts for the fault properties are *NF* and *R*. The normal and the reverse faults have conjugate shear discontinuities or axial surfaces *JI* and *GF* and having the same properties as the bulk material. The normal fault and the axial surfaces are dipping at γ_i and θ_i with the subscript i set either to a or to p, Fig. 1. The subscript a and p means active and passive, a classical terminology in geotechnics to define the regions collapsing in extension and compression, respectively.

We have thus defined the three structural regions. It is the half-graben (HG) defined by the region *HIJ* which is the driver for the gravity instability. It presses the resisting sliding block (SB) seaward up to the compressive domain where thrusting occurs with the hanging wall (HW) defined by the region *EFG*. This motion is with respect to the immobile frontal seaward region (FS) and the back, landward region (BL). The mechanical approach presented in the last part of this section provides the means to compute the position of the six points *E*, *F*, *G* and *H*, *I*, *J*.

The material is submerged and any point $\underline{x}$ within the wedge has a sea bed at the depth $D(\underline{x})$, Fig. 1. The second or vertical coordinate axis points upward with an origin at the sea surface. The fluid pressure p at $\underline{x}$ and the corresponding fluid overpressure Δp, difference with the hydrostatic pressure, are

$$p = g[-\lambda\,\rho x_2 + (\rho_f - \rho\lambda)D] \quad \text{and} \quad \Delta p = -\Delta\lambda\,\rho g(x_2 + D)\,, \tag{1}$$

in which ρ and ρ_f are the volumetric mass of the saturated solid and of the fluid, respectively. The two scalars λ and $\Delta\lambda$ are the fluid pressure ratio and the overpressure ratio defined by Hubbert & Rubey (1959)

$$\Delta\lambda = \lambda - \lambda_{\text{hydro}}, \quad \text{with} \quad \lambda_{\text{hydro}} = \rho_f/\rho \quad \text{and} \quad \Delta\lambda_{\text{Max}} = 1 - \rho_f/\rho. \tag{2}$$

The maximum value $\Delta\lambda_{\text{Max}}$ is introduced for further reference. The value of the pressure ratios λ_i could differ in the bulk material, in the detachment, as well as in the normal and thrust faults. The subscript i is thus either B or D as for the frictional properties. The history and present-day conditions which could explain these differences are not discussed in this contribution.

It should be stressed that there are different definitions of λ in the literature due to the selection of various coordinate systems. These different parametrizations lead to difficulties when comparing the various predictions. Some definitions have been discussed at length in the appendix of paper 1 and two new definitions are presented in the Supporting Information.

2.2 Application of Limit Analysis

The first step of the kinematic approach of Limit Analysis (Chen 1975; Salençon 2002) consists in the definition of the virtual velocity field associated to the collapse mechanism just described. This velocity is virtual since it may not be the exact one and corresponds, as in our particular case, to a simplification proposed to obtain an analytical solution.

The proposed virtual velocity field is uniform in each of the three structural domains and denoted $\underline{\hat{U}}_{\text{HG}}$, $\underline{\hat{U}}_{\text{SB}}$ and $\underline{\hat{U}}_{\text{HW}}$. The superposed hat is to remind the reader of the virtual character of the piecewise uniform field. This piecewise uniform property implies that there are discontinuities across the two axial surfaces (*JI* and *GF*) and of course across the detachment (*JG*) and the two faults (*JH* and *GE*). The set of these discontinuities is denoted Σ. The difference between the velocities on the two sides of a discontinuity in Σ is the velocity jump denoted $\underline{\hat{J}}$ (discontinuities are oriented in Fig. A1).

One further property is required for this velocity field: velocity jumps are not parallel to the corresponding discontinuity but are oriented at the angle φ_i corresponding to the discontinuity friction angle. The theoretical reasons for this choice, which is counter-intuitive for a naturalist, were discussed at length in Maillot & Leroy (2006) and paper 1, as well as in Cubas *et al.* (2008, Electronic Supplement). The immediate consequence of this orientation selection is the introduction of a set of constraints which enforce that the sense of shear on the axial surfaces and the faults is indeed the ones presented in Fig. 1:

$$\begin{aligned}
&\varphi_B + \varphi_D + \beta < \theta_a < \pi\,, \quad \varphi_{NF} - \varphi_D - \beta < \gamma_a < \pi,\\
&\varphi_B + \varphi_{NF} < \gamma_a + \theta_a < \pi\,, \quad -\beta < \theta_p < \pi - \varphi_B - \beta - \varphi_D,\\
&\beta < \gamma_p < \pi + \beta - \varphi_R + \varphi_D\,, \quad 0 < \gamma_p + \theta_p < \pi - \varphi_B - \varphi_R,
\end{aligned} \tag{3}$$

as it is demonstrated in Appendix A1 with the construction of two hodographs.

The second step in Limit Analysis is the application of an integral expression (weak form) of mechanical equilibrium. Following Pons & Leroy (2012), it states the equality between the effective external power and the effective internal power

$$\mathcal{P}'_{\text{ext}}(\underline{\hat{U}}) = \mathcal{P}'_{\text{int}}(\underline{\hat{U}})\,, \ \forall\,\underline{\hat{U}} \tag{4}$$

for any virtual velocity field having the properties described above. The effective external power is

$$\mathcal{P}'_{\text{ext}}(\underline{\hat{U}}) = \int_{\Omega_t} \rho\underline{g}\cdot\underline{\hat{U}}\,\mathrm{d}V + \int_{\Sigma} p_\Sigma \underline{n}\cdot\underline{\hat{J}}\,\mathrm{d}S\,. \tag{5}$$

The first term is the power of the gravity field on the virtual velocity, with $\underline{g}$ denoting the gravity acceleration. The second term corresponds to the power of the velocity discontinuities (normal component, with the normal vector denoted $\underline{n}$ and pointing towards the positive side) on the fluid pressure, considered as an external field for the set Σ defined above. The calculation of $\mathcal{P}'_{\text{ext}}(\underline{\hat{U}})$ is technical and this exercise is postponed to Appendix A1 where the general expression (A3) is proposed.

The internal effective power $\mathcal{P}'_{\text{int}}$ in (4) results in our particular case from the power of the effective stress vectors on the velocity jumps of the set Σ. Since the exact stress field and consequently the stress vectors are unknowns, it is proposed in the kinematic approach of Limit Analysis to construct an upper bound to this internal power. It is defined as the maximum resisting power and is obtained by integration along the discontinuities of Σ

$$\mathcal{P}'_{\text{mr}}(\underline{\hat{U}}) = \int_{\Sigma} \hat{J} C \cos\varphi \, \mathrm{d}S, \tag{6}$$

where C and φ are the cohesion and friction angle of the discontinuity. Again, the detailed expression for this quantity is found in Appendix A1, eq. (A4). The justification for the integrand in eq. (6) is found in Maillot & Leroy (2006). Note that if the cohesion is null, $\mathcal{P}'_{\text{mr}}$ is null. Frictional resistance is nevertheless accounted for in the gravity term of the external power (5) which is developed explicitly in eq. (A3).

Combine now eq. (4) and the fact that eq. (6) is a bound to the internal power to obtain the inequality

$$\mathcal{P}'_{\text{ext}}(\underline{\hat{U}}) - \mathcal{P}'_{\text{mr}}(\underline{\hat{U}}) \leq 0\,. \tag{7}$$

The stability conditions controlling the onset of the gravity instability are as follows. If this inequality is strictly enforced for all choices of velocity field, there is no gravity instability. If there are collapse mechanisms for which the effective external power and the maximum resisting power are identical, they define the conditions for the onset of a gravity instability. If the effective external power is found to be greater than the maximum resisting power, the corresponding collapse mechanism represents a dynamic instability. Note that the kinematic approach of Limit Analysis does not warrant a unique collapse mechanism at the onset of instability.

For all practical purposes, the procedure to determine the collapse mechanism consists in maximizing the difference in the left-hand side of eq. (7). The mechanism associated with this maximum is considered to be dominant, since it is the closest to the instability condition if the difference in eq. (7) is negative. This maximum is found by varying the dips $\gamma_a, \theta_a, \gamma_p, \theta_p$ and the positions of points J and G or, equivalently, the positions of the six points E, F, G and H, I, J. The numerical procedure is the same as the one presented in Cubas *et al.* (2008, Appendix).

3 VALIDATION FOR AN INCLINED LAYER

The complex topography of our general prototype is now planar, parallel to the detachment ($\alpha = \bar{\beta} = -\beta$), so that the prototype is forming an inclined layer of thickness h (Fig. 2a). All materials are cohesionless so that the maximum resisting power in eq. (6) is zero. The normal fault and thrust ramp are assumed to have the same friction angle and fluid pressure ratio as the bulk material: $\varphi_{NF} = \varphi_R = \varphi_B$, $\lambda_{NF} = \lambda_R = \lambda_B$. The solution of Limit Analysis for this simplified problem is now presented, and is compared with known results and with experimental data for granular materials.

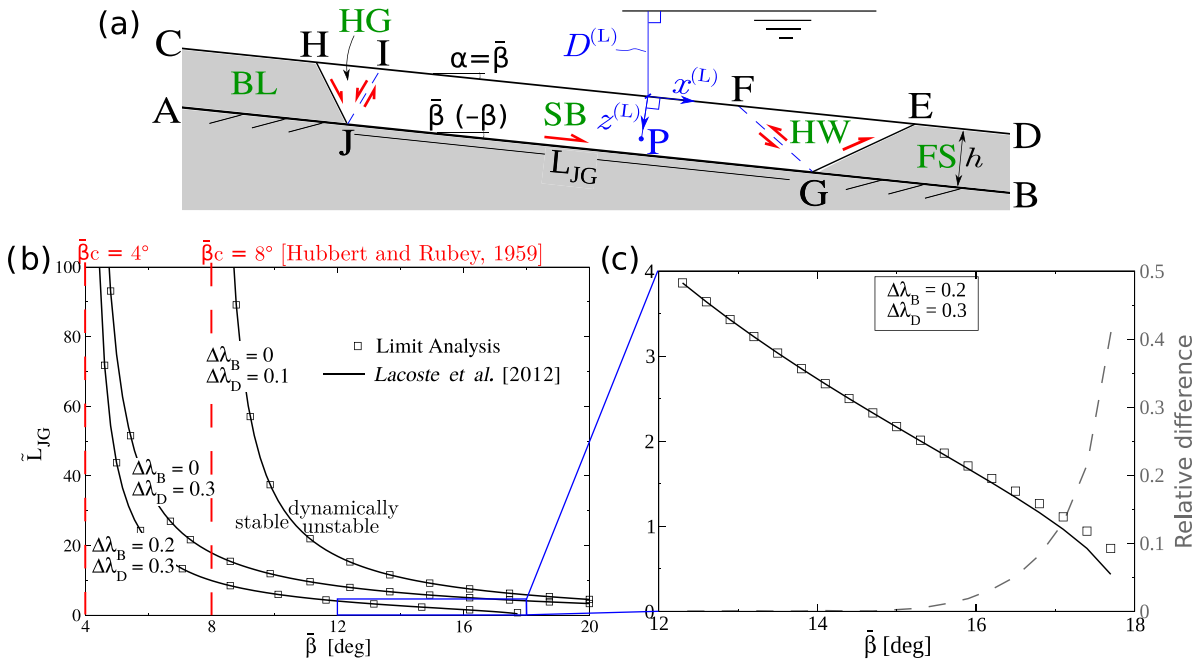

Figure 2. The critical length of the transitional region for the inclined layer presented in (a). (b) Comparison of the predictions of Limit Analysis (symbols) and the analytical solutions proposed in Lacoste *et al.* (2012). The vertical dashed lines present the critical dips for an infinite length. (c) Zoom for small values of the transitional region length and layer dip with in addition the relative difference between the two predictions (grey dashed curve).

The general expression (A3) in Appendix A1 for $\mathcal{P}'_{\text{ext}}$ is simplified greatly for this prototype and the stability condition (7) reads

$$\tilde{\mathcal{P}}'_{\text{ext}} = \mathcal{A}\,\tilde{L}_{JG} + \mathcal{B} \leq 0\,,$$

with $\mathcal{A} = \big[-\Delta\lambda_{\text{Max}}\sin(\beta+\varphi_D) + \Delta\lambda_D\sin(\varphi_D)/\cos\beta\big]$,

and
$$\begin{aligned}\mathcal{B} = \frac{1}{2}\Delta\lambda_{\text{Max}}\Big[&\big[\cot(\gamma_a+\beta)+\cot(\theta_a-\beta)\big]\sin(\gamma_a-\varphi_B)\tilde{U}_{\text{HG}}\\ &-\big[\cot(\theta_p+\beta)+\cot(\gamma_p-\beta)\big]\sin(\gamma_p+\varphi_B)\tilde{U}_{\text{HW}}\\ &+\big[\cot(\theta_a-\beta)+\cot(\theta_p+\beta)\big]\sin(\beta+\varphi_D)\Big]\\ &+\frac{1}{2}\Delta\lambda_B\frac{\sin(\varphi_B)}{\cos\beta}\Big[\frac{\tilde{U}_{\text{HG}}}{\sin(\gamma_a+\beta)}+\frac{\tilde{J}_{JI}}{\sin(\theta_a-\beta)}+\frac{\tilde{U}_{\text{HW}}}{\sin(\gamma_p-\beta)}+\frac{\tilde{J}_{GF}}{\sin(\theta_p+\beta)}\Big]\,.\end{aligned} \tag{8}$$

The superposed tilde identifies dimensionless quantities obtained by division of physical quantities with reference values, $\rho g h$ for stresses, h for lengths. The virtual velocities are normalized by the sliding block velocity $\hat{U}_{\text{SB}}$ and the superposed tilde marks also this division. The relations between the various velocities are constructed in Appendix A1 and the final result is

$$\begin{aligned}\frac{\tilde{U}_{\text{HG}}}{\sin(\theta_a-\varphi_B-\beta-\varphi_D)} &= \frac{1}{\sin(\theta_a+\gamma_a-\varphi_{NF}-\varphi_B)} = \frac{\tilde{J}_{JI}}{\sin(\gamma_a+\beta-\varphi_{NF}+\varphi_D)}\,,\\ \frac{\tilde{U}_{\text{HW}}}{\sin(\theta_p+\varphi_B+\beta+\varphi_D)} &= \frac{1}{\sin(\theta_p+\gamma_p+\varphi_R+\varphi_B)} = \frac{\tilde{J}_{GF}}{\sin(\gamma_p-\beta+\varphi_R-\varphi_D)}\,.\end{aligned} \tag{9}$$

It should be noted that the sea depth does not influence the stability condition in eq. (8). It is only the fluid pressure ratios which matter for the fluid contribution. The same remark applies in the next section.

The term $\mathcal{A}\,\tilde{L}_{JG}$ in eq. (8) is independent of the fault dips and is interpreted as the contribution of the sliding block to the effective, external work. The term $\mathcal{B}$ is independent of the sliding block extent and corresponds to the contributions of the upslope half-graben and the downslope hanging wall.

The zero cohesion implies that the maximum resisting power $\mathcal{P}'_{\text{mr}}$ in eq. (6) is also zero and, according to the stability condition eq. (7), that the onset of gravity instability is defined by

$$\text{Max}\big[\tilde{\mathcal{P}}'_{\text{ext}}(\beta,\gamma_a,\theta_a,\gamma_p,\theta_p,\tilde{L}_{JG})\big] = 0\,, \tag{10}$$

having limited the list of arguments to the geometrical variables. The relation for $\tilde{\mathcal{P}}'_{\text{ext}}$ in eq. (8) is affine and the sign of the scalar $\mathcal{A}$ is determinant to find the optimum geometrical variables maximizing eq. (10). If $\mathcal{A}$ is positive, the optimum length $\tilde{L}_{JG}$ is infinite. If $\mathcal{A}$ is negative, there is an optimum length $-\mathcal{B}/A$ if $\mathcal{B}$ is positive. A negative maximum $\mathcal{B}$ would mean stability. The sign of $\mathcal{A}$ is conveniently examined by introducing the critical β_c for which this term is zero:

$$\beta_c = -\frac{1}{2}\sin^{-1}\left[\left(1-2\frac{\Delta\lambda_D}{\Delta\lambda_{\text{Max}}}\right)\sin(\varphi_D)\right] - \frac{1}{2}\varphi_D\,. \tag{11}$$

The layer dip is negative and if β is less than β_c (larger in absolute value), the scalar $\mathcal{A}$ is positive. The maximum $\tilde{\mathcal{P}}'_{\text{ext}}$ is then associated to an infinitely long layer. For such values of β, the system is dynamically unstable. Of more interest here are the cases for which β is greater than β_c (smaller in absolute value). The maximum in eq. (10) is then evaluated as follows: (i) maximize $\mathcal{B}$ with respect to γ_a, θ_a, γ_p and θ_p subjected to the constraints in eq. (3), and thus determine the optimum dips of the half-graben and the hanging wall; (ii) calculate the collapse length $\tilde{L}_{JG}$ which ensures the instability condition (10) if the maximum $\mathcal{B}$ is positive.

The new result here is that the length of the sliding block is simply determined by the ratio of two scalars. The denominator $\mathcal{A}$ is only function of the detachment dip and friction angle and of the overpressure ratio. The numerator $\mathcal{B}$ is function of the geometry, the frictional properties and the overpressures in the half-graben and in the hanging wall. The change of sign (negative to positive) of the numerator signals a dynamic instability starting with the longest wave-length mode possible. This change of sign could be due, for example, to a variation in the detachment overpressure or frictional properties, or to a rotation of the detachment dip.

3.1 Comparison with other analytical results

Hubbert & Rubey (1959) considered the classic stability analysis of an infinite frictional, cohesionless layer above a fluid overpressured base and determined the critical slope, their eq. (117)

$$\bar{\beta}_c = \tan^{-1}\big[(1-\lambda_D^{(L)})\tan(\varphi_D)\big], \tag{12}$$

which is expressed here in terms of the overpressure ratio $\lambda_D^{(L)}$ defined in Lacoste *et al.* (2012)

$$\lambda^{(L)} = \frac{p_f^{(L)} - \rho_f g(D^{(L)} + z^{(L)}\cos\alpha)}{(\rho-\rho_f)gz^{(L)}\cos\alpha}\,. \tag{13}$$

Table 1. Geometrical, material parameters and fluid pressure ratios for the stability analyses (validation and application to the Niger Delta).

Notation	Definition	Value/range [Sections 3.1 and 4.1]	Value/range [Section 3.2]	Value/range [Section 4.2]	Unit
α	Topographic slope	Variable	6.7	1[b]	deg
β	Detachment dip	Variable	−6.7	1.5[b]	deg
h	Reference height	1	4×10^{-5}	3[b]	km
L_{JG}	Collapse length	Variable	–	100–200	km
φ_a	Friction angle ($a = B, AS, NF, R$)[a]	30	50–63	30[c]	deg
φ_D	Detachment friction angle	10	10	10[c]	deg
C_a	Cohesion ($a = B, AS, NF, R$)[c]	$(0, 0.1) \cdot \rho g h$	0	$(0–7) \cdot 10^6$	Pa
C_D	Detachment cohesion	0	0	0	Pa
ρ_f	Fluid phase density	1000	1000	1030	kg m^{-3}
ρ	Saturated rock density	2000	2000	2400[b]	kg m^{-3}
λ_{hydro}	Hydrostatic pressure ratio ($= \rho_f/\rho$)	0.5	0.5	0.42	–
$\Delta\lambda_B$	Bulk overpressure ratio	0.0–0.2	−0.5–0.5	0.3–0.5	–
$\Delta\lambda_D$	Detachment overpressure ratio	0.1–0.3	$\Delta\lambda_B$	0.5–0.57	–

[a]Notation: *B*, Bulk; *AS*, Axial surface; *NF*, Normal fault; *R*, Ramp.
[b]Parameters are from Bilotti & Shaw (2005).
[c]Parameters are from Krueger & Grant (2011) and Suppe (2014).

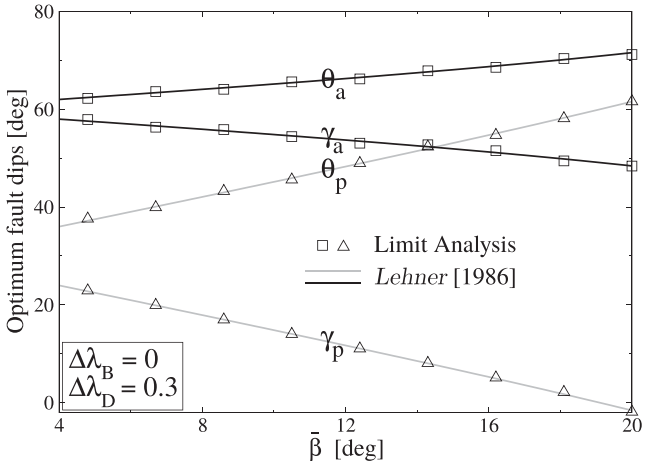

Figure 3. Comparison of fault dips (γ_a, θ_a, γ_p and θ_p) for the active (or upslope, extensional) and passive (or downslope, compressive) collapses. The solid lines are the theoretical dips of the CCW theory provided in the Supporting Information Section ES2 for the sake of completeness.

The distance $D^{(L)}$ and the coordinate $z^{(L)}$ are defined in Fig. 2(a). Further information on the fluid pressure ratios is found in the Supporting Information. This solution (12) coincides exactly with our solution (11). This can be verified by incorporating into (12) the definition of $\lambda_D^{(L)}$ in terms of λ_D, Supporting Information eq. (ES1.2), rearrange the trigonometric functions and finally use eq. (2) to obtain eq. (11).

The collapse extent $\tilde{L}_{JG}$ is now compared with the analytical results of Lacoste *et al.* (2012, eq. (9)) which is presented in details in the Supporting Information. For that purpose, the values of $\bar{\beta}_c = 4^\circ$ and 8° corresponding to $\Delta\lambda_D = 0.3$ and 0.1 are selected. Their associated critical lengths are infinite shown by the vertical dashed lines in Fig. 2(b). The other material property values are summarized in the third column of Table 1.

The comparison of the Limit Analysis (symbols) and analytical results (curves) are presented in Figs 2(b) and (c). The two solutions are very close for the three sets of detachment and bulk overpressure ratios. Differences become important at low values of $\tilde{L}_{JG}$, corresponding to large slopes ($\bar{\beta} \geq 16^\circ$) as shown by the relative difference between these two predictions (grey dashed curve) in Fig. 2(c). Note that, as expected, the range of critical detachment dips $\bar{\beta}$ for the finite collapse length is always greater than the critical dip $\bar{\beta}_c$ for the infinite collapse length. These curves also demonstrate that if an experiment is performed by increasing the detachment dip $\bar{\beta}$ up to collapse, it will occur for the longest length available for slip. If the experiment is conducted by increasing $\Delta\lambda_D$, keeping a constant dip $\bar{\beta}$, then the onset collapse occurs also with the longest length available.

The comparison of the fault dips (γ_a, θ_a, γ_p and θ_p) according the two approaches is presented in Fig. 3, the dips for the Lacoste *et al.*'s (2012) solution being obtained from the Mohr's construction of Lehner (1986) for the active and passive Rankine stress states. The interesting result of eq. (8) is that the dip optimization is decoupled from the selection of the length since it is due to the scalar $\mathcal{B}$ only. As a consequence, the dips are also the ones predicted by the CCW theory, as it is checked by numerical means and shown in Fig. 3.

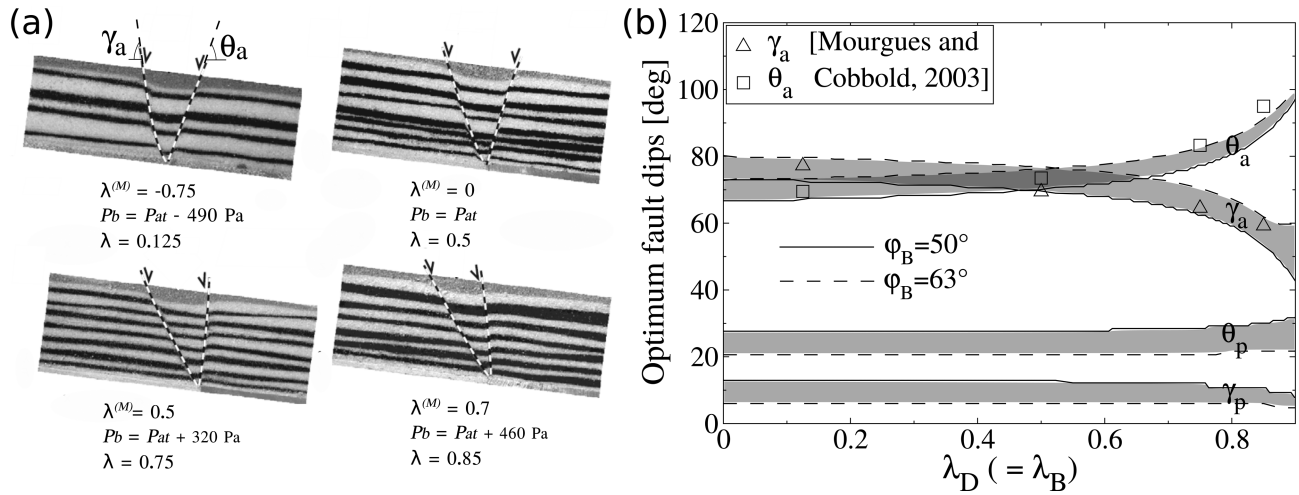

Figure 4. The validation of the Limit Analysis by comparing the fault dips with observations from the sandbox experiments. (a) The active faults formed by different air pressures through the sand packs, modified after Mourgues & Cobbold (2003). (b) The comparison of active fault dips (γ_a, θ_a) from experiments (triangle and square symbols) and predictions from the Limit Analysis (grey zones between solid and dashed curves) as function of fluid pressure ratio.

3.2 Validation with sandbox experiments in fluid overpressured conditions

The dips of the active faults predicted with the Limit Analysis are now validated by comparing the predictions with the observations done on the sandbox experiments of Mourgues & Cobbold (2003) in which fluid overpressures are obtained with compressed air. The experimental setup consists of a rectangular box in which flat sand packs are built with a length of 40 cm, a width of 20 cm, and a height of 4 cm. The box is inclined at $\bar{\beta} = 6.7^\circ$. The sand density ρ_s is 1700 kg m^{-3}, the internal friction coefficient is 1.18 ($\varphi_B = 50^\circ$) and the bulk cohesion C_B is in the range 12 to 72 Pa, all information provided by the authors. The sand pack rests on two overlapping sieves. Beneath the sieves a pressure chamber provides a uniform air pressure (p_b) at the base of the sand body. The top is maintained at the atmospheric pressure p_{at} so that air flows through the sand in a direction perpendicular to the slope. With this setup, the pressure ratios on the detachment and in the sand are the same $\lambda_B^{(M)} = \lambda_D^{(M)}$ (Mourgues & Cobbold 2003, 2006b; Lacoste *et al.* 2012; Pons & Mourgues 2012). Definition of $\lambda^{(M)}$ in terms of λ is given, again, in Section ES1 of the Supporting Information. By slowly moving one of the sieves in extension, conjugate normal faults are generated when a discontinuity is created at the base (Fig. 4a). For each of the four experiments, the corresponding value of λ is given in Fig. 4(a).

Limit analysis provides not only the orientations of the active faults but also the passive fault dips as well as the length of the translational domain. However, since the latter data was not published, the comparison is limited to the active faults dips. Furthermore, to complete our data set, we assume that the detachment has zero cohesion and we choose $\varphi_D = 10^\circ$ to obtain indeed slip for the imposed dip at 6.7°.

The experimental results and our predictions are presented in Fig. 4(b) where the fault dips are drawn versus the fluid pressure ratio $\lambda_D (= \lambda_B)$. The experimental results show that the normal fault dip γ_a (triangle symbols) decreases and the axial surface dip θ_a (square symbols) increases with the increase of the fluid pressure ratio. The internal friction angle φ_B inferred from these dips ranges between 52° ($\mu_B = 1.3$) and 68° ($\mu_B = 2.5$) at vanishing effective normal stress (Mourgues & Cobbold 2003, fig. 6c). The theoretical results obtained for φ_B between 50° (solid curves) and 63° (dashed curves) are shown as grey ranges. They match well the experimental dips, except for θ_a at $\lambda_B = \lambda_D = 0.85$. We conclude that the series of four experiments are well captured by the Limit Analysis. Another interesting observation is that the passive fault dips (γ_p, θ_p, Fig. 4b), compared to the active fault dips (γ_a, θ_a), are not varying much until the fluid pressure ratio is close to 0.8.

4 APPLICATION TO THE OFFSHORE NIGER DELTA

The prototype is now wedge shaped to approximate the cross-section of the offshore Niger Delta. The collapse mechanism is identical to the one previously considered. The fluid overpressures are determined by requiring that the observed surface and detachment dips, α and β, correspond to conditions for the onset of instability. The differences between the predicted fluid overpressures and the ones previously determined (Bilotti & Shaw 2005) are discussed to conclude the section.

4.1 Stability conditions

The stability condition in eq. (7) is based on the difference between the effective external power and the maximum resisting power which now read

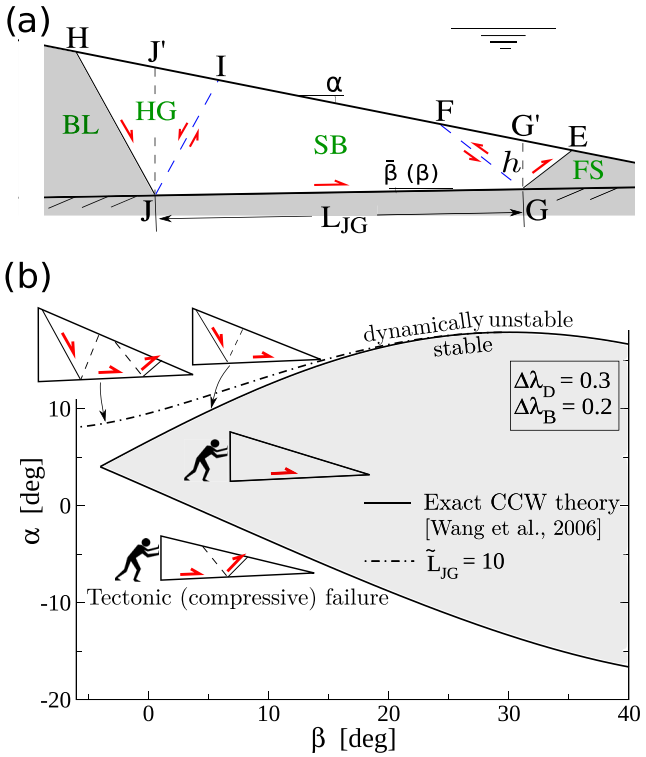

Figure 5. The collapse mechanism for a wedge with three interacting structural domains, (a), and comparison with the CCW theory, (b). The solid curves bound the stability domain and account for the corrections proposed by Wang *et al.* (2006). The proposed critical surface slope (dash-dotted curve) due to the interaction is function of the collapse length set here to $L_{JG} = 10h$.

$$\begin{aligned}\tilde{\mathcal{P}}'_{\text{ext}}(\underline{\tilde{U}}) = \Delta\lambda_{\text{Max}}\big[&\tilde{S}_{\text{HG}}\tilde{U}_{\text{HG}}\sin(\gamma_a - \varphi_{NF}) - \tilde{S}_{\text{SB}}\sin(\beta + \varphi_D) - \tilde{S}_{\text{HW}}\tilde{U}_{\text{HW}}\sin(\gamma_p + \varphi_R)\big] \\ &+ \Delta\lambda_{NF}\,\tilde{S}_{JJ'H}\tilde{U}_{\text{HG}}\frac{\sin(\varphi_{NF})}{\cos(\gamma_a)} + \Delta\lambda_B\,\tilde{S}_{JJ'I}\tilde{J}_{JI}\frac{\sin(\varphi_B)}{\cos(\theta_a)} + \Delta\lambda_B\,\tilde{S}_{GG'F}\tilde{J}_{GF}\frac{\sin(\varphi_B)}{\cos(\theta_p)} \\ &+ \Delta\lambda_R\,\tilde{S}_{GG'E}\tilde{U}_{\text{HW}}\frac{\sin(\varphi_R)}{\cos(\gamma_p)} + \Delta\lambda_D\,\tilde{S}_{JJ'G'G}\frac{\sin(\varphi_D)}{\cos\beta}\,,\end{aligned} \tag{14}$$

and

$$\begin{aligned}\tilde{\mathcal{P}}'_{\text{mr}}(\underline{\tilde{U}}) = &\tilde{C}_D\tilde{L}_{JG}\cos(\varphi_D) + \tilde{C}_{NF}\tilde{L}_{JH}\cos(\varphi_{NF})\tilde{U}_{\text{HG}} + \tilde{C}_B\tilde{L}_{JI}\cos(\varphi_B)\tilde{J}_{JI} \\ &+ \tilde{C}_R\tilde{L}_{GE}\cos(\varphi_R)\tilde{U}_{HW} + \tilde{C}_B\tilde{L}_{GF}\cos(\varphi_B)\tilde{J}_{GF}\,.\end{aligned} \tag{15}$$

These two equations correspond to a normalized and a dimensionless version of eqs (A3) and (A4) in Appendix A1. Normalization and dimensional analysis are done as in the previous section except for the reference length which is now h, the thickness of the sediments above point G at the wedge toe, Fig. 5(a). Note that the collapse mechanism position with respect to sea level, set by the position of point G, is immaterial, since the external power is only function of the fluid pressure ratios, as discussed in the previous section. The surfaces $S_{JJ'H}$, $S_{JJ'I}$, $S_{GG'F}$, $S_{GG'E}$ and $S_{JJ'G'G}$ are the surfaces based on the points G' and J' found on the topography at the apex of points G and J, respectively. Expressions for these surfaces are provided in Appendix A3 for the sake of completeness. The normal fault JH and the thrust ramp GE have the same fluid pressure ratio and material properties as the bulk material. The relations between the various virtual velocities provided in eq. (9) still apply to this prototype.

It is proposed to build a stability map in the (α, β) plane based on the stability condition in eq. (7) for given values of the pressure ratios and the sliding block length. The following procedure is conducted for every set (α, β) to decide if the corresponding wedge is stable or not. We first maximize the difference in eq. (7) with respect to the four dips γ_a, θ_a, γ_p and θ_p, respecting the constraints in eq. (3). Second, if the maximum difference is negative, the wedge is said stable, otherwise unstable. Note that a positive difference marks a dynamic instability. The result of the procedure is the dash-dotted curve in Fig. 5(b) obtained for the data corresponding to the third column in Table 1 and to $\tilde{L}_{JG} = 10$.

The stability conditions due to the exact CCW theory (Wang *et al.* 2006) for cohesionless materials (grey area) have also been plotted in this Fig. 5(b). Within the grey area, the wedge slides along the whole detachment without internal deformation either by its self-weight or by tectonic compression. The lower boundary of this domain corresponds to the stability limit of accretionary wedges in the compressive

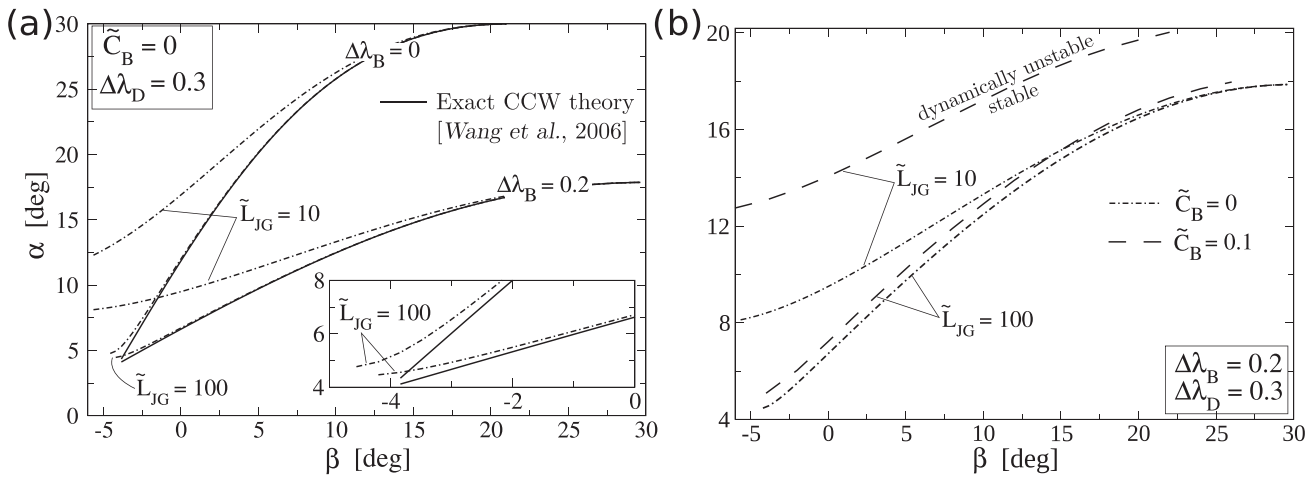

Figure 6. (a) The critical surface slope as function of the detachment dip for the detachment activation length $\tilde{L}_{JG}$ set to 10 or 100 and the bulk overpressure ratio $\Delta\lambda_B$ set to 0 or 0.2 (dash-dotted curves). The bulk cohesion is zero. The solid curves are the upper stability limits of the exact CCW theory corresponding to $\tilde{L}_{JG} \to \infty$. In (b), comparison of the predictions with zero cohesion and with $\tilde{C}_B$ equal to 0.1 (dashed curves).

regime. Of more interest here is the upper boundary of the grey domain corresponding to gravity instability (Mourgues *et al.* 2014). This upper limit is very close to our predictions (dash-dotted curve) for β larger than 25°. The difference between our predictions and the exact CCW theory is more apparent for small values of β with a maximum of approximately 5° in the topographic slope.

The stability of our prototype is further explored with the help of Fig. 6(a), presenting the critical curves of the exact CCW theory (solid curves) and those obtained for $\tilde{L}_{JG} = 10$ and 100 (dash-dotted curves) at the bulk overpressure ratio $\Delta\lambda_B = 0$ and 0.2. Changing $\tilde{L}_{JG}$ from 10 to 100 results in a decrease of the critical topographic slope. The value of 100 is sufficiently large for the exact CCW theory, corresponding to the limit of infinite $\tilde{L}_{JG}$, to be accurate enough. Increasing the bulk overpressure ratio from zero to 0.2 reduces significantly the critical topographic slopes but the difference between the Limit Analysis and the CCW theory is still apparent up to a detachment dip of 20°. The role of cohesion is now discussed with the help of Fig. 6(b) and the comparison with the CCW theory is of course not possible anymore. The dimensionless cohesion of 0.1 (physical value of 2 MPa, Table 1, third column) has little influence for the larger length $\tilde{L}_{JG}$. For the smaller value of 10, the difference in α for a small value of β, say 5°, is close to 5°.

In summary, the interaction between the three regions of the collapsing wedge increases the stability limit of the wedge to larger topographic slopes. The physical explanation is that the frontal thrust offers an additional resistance to the gravity instability, which is therefore triggered for a larger surface slope. This effect is greater for cohesive materials and at low fluid pressures. This effect becomes insignificant for $\tilde{L}_{JG}$ tending to infinity and, for practical purposes, a dimensionless length greater than 100 is sufficiently large for the CCW theory to be accurate enough.

4.2 Stability analysis of Niger Delta

The structure of the Niger Delta is characterized by normal faulting in the thickest part near the coast, and by fold-and-thrust belts in the deepest, thinnest part, further offshore (Fig. 7a). This is broadly interpreted as a seaward gravity instability of the sedimentary basin (Agada Formation) above a substratum of overpressured shale (Akata Formation; Wu & Bally 2000). In this last work, it was shown that the interpretation of recent seismic lines in the shale domain has revealed that what was interpreted earlier as shale diapirs should be seen as the result of thrusting. Although density inversion should not be disregarded, this information confirms the idea that the Niger Delta could be interpreted to first order as a frictional wedge. The detachment has certainly a complex structure within the Akata Formation and, following Bilotti & Shaw (2005) and Suppe (2014), we propose to represent this complex zone by a single, planar detachment from the extensional domain to the thrusting domain. This detachment is dipping at $\beta \sim 1.5°$ (Fig. 7b) which corresponds to the average value found by Bilotti & Shaw (2005) from 10 sections through the frontal toe with an average taper of 2.5° and an average surface slope $\alpha \sim 1°$ (Fig. 7b). These topographic slope and detachment dip are kept constant in the calculations presented in this section. The length L_{JG} of the active detachment is estimated to be in the range of 100–200 km from the works of Corredor *et al.* (2005) and Leduc *et al.* (2012) (Fig. 7a), and the height h of sediments at the frontal thrust belt is about 3 km. The dimensionless length $\tilde{L}_{JG}$ is thus between 30 and 70, a range for which the interaction of the three structural domains cannot be disregarded according to the results of the previous section.

Mechanical properties of shales have been studied in the laboratory. Triaxial tests on Tournemire shales in Southern France (Bonnelye *et al.* 2016) point to a friction coefficient of 0.2–0.3. This coefficient could be larger (0.4) for gouge materials depending on the organic content and of course on the rate of straining (Kohli & Zoback 2013). *In situ* measurements by leak-off tests for the Gulf of Mexico point to a bulk friction coefficient in the range 0.25–0.3 (Suppe 2014). The same author suggests that the fault in shales should have a smaller coefficient, ~0.2, a value which is adopted here. Our bulk material is heterogeneous (sand and shale alternance) and we use a value of 0.6, consistent

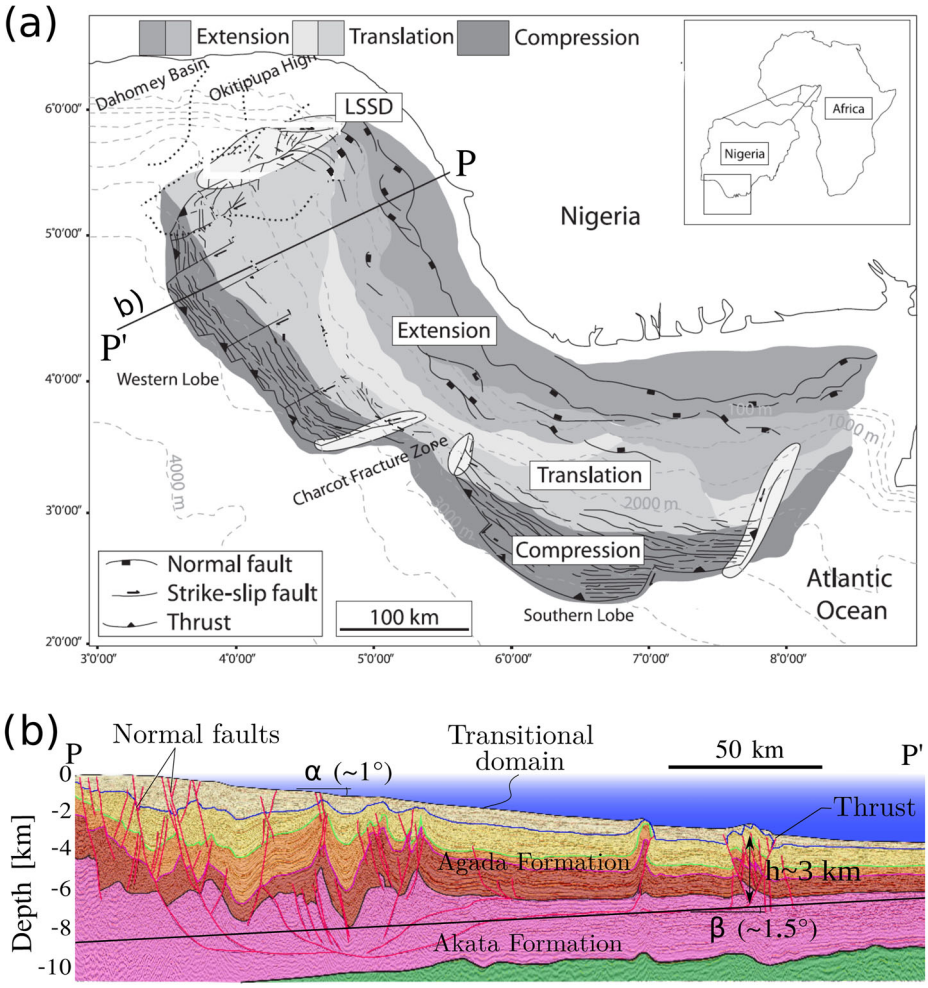

Figure 7. (a) Overview of offshore Niger Delta structural domains, modified from Leduc *et al.* (2012). (b) Cross-section PP′ (Morgan 2006) with the three structural domains and the position of the assumed detachment surface in the Akata formation, adopted from Butler (2010).

with upper crustal rocks (Byerlee 1978). For the same reason, we choose a bulk cohesion of 7 MPa ($\tilde{C}_B = 0.1$) while the detachment is assumed cohesionless. The fluid pressure is hydrostatic ($\Delta\lambda_B = 0$) at depths down to 2.3 km (fluid-retention depth) from the sea bed, and the pressure increases closely to lithostatic pressure ($\Delta\lambda_B \leq 0.58$) if the depth is greater than 3 km (Krueger & Grant 2011). However, for sake of simplicity in this contribution, we keep the overpressure ratios constant and vary them in the range of [0.3, 0.5] and [0.5, 0.57] for the bulk and the detachment overpressure ratios, respectively. All parameters are summarized in Table 1 (fifth column).

Our stability predictions are now presented in Fig. 8 where the two graphs are constructed in the space spanned by the effective friction coefficients of the bulk material and the detachment. They are defined by Hubbert & Rubey (1959) as $\mu_i' = \tan(\varphi_i)(1 - \lambda_i^{(L)})$ with the expression of $\lambda^{(L)}$ found in eq. (ES1.2) of the Supporting Information. The approximation of $\cos^2\alpha$ by one is proposed in view of the very low surface slope of the Niger Delta and the two effective friction coefficients have the final expression

$$\mu_i' = \tan(\varphi_i)\left(1 - \frac{\Delta\lambda_i}{\Delta\lambda_{\text{Max}}}\right), \quad i = \text{B, D.} \tag{16}$$

The stability limits in the space spanned by μ_B' and μ_D' are determined for three values of the dimensionless detachment activation length $\tilde{L}_{JG}$ of 30, 70 and 10^4. The stability predictions for the last value correspond within numerical error to the CCW theory and are referred to as the predictions for $\tilde{L}_{JG} \to \infty$ in what follows.

Consider now Fig. 8(a) obtained with zero cohesion. The differences in the three stability limit curves confirm the importance of the finite extent of the transitional domain. The Niger Delta stability conditions should lie within the grey area, bounded by the solutions for the dimensionless length of 30 and 70. Note that this grey area has a cone shape with a tip at $\mu_B' = 0.017$. For this frictional value, any detachment friction coefficient and any transition length is possible. This singular result points to the conclusion that the bulk material with the topographic slope $\alpha = 1^\circ$ cannot remain stable with a bulk friction coefficient lower than 0.017. The grey cone thus partitions the stability map in four regions. On top of the grey area, the wedge is stable if $\tilde{L}_{JG}$ does not exceed 70. Below the grey cone, the wedge is unstable unless

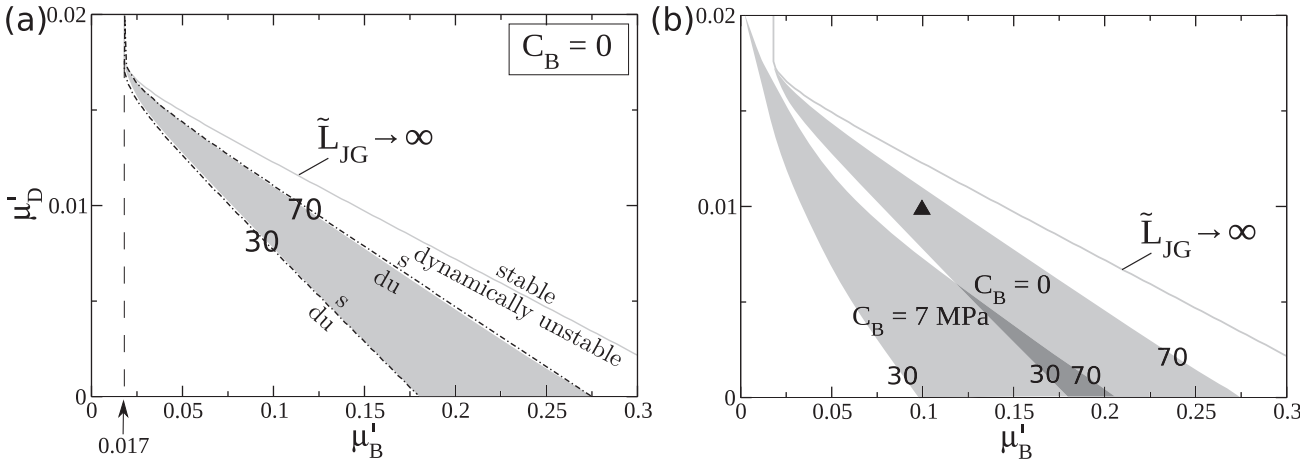

Figure 8. (a) The stability transition for the offshore Niger Delta in the space spanned by the bulk and detachment effective friction coefficient. The grey region is where this transition should be found in view of the uncertainty of the detachment activation length, $\tilde{L}_{JG} = 30-70$. (b) Influence of bulk cohesion on the shape and position of the grey region. The $\tilde{L}_{JG} \to \infty$ curve is identical to the CCW prediction. Black triangle ($\mu'_B = 0.1, \mu'_D = 0.01$) indicates the central position within the cone for zero cohesion.

this length is smaller than 30. To the left of $\mu'_B = 0.017$, slope is definitely unstable. The solution for the Niger Delta should be within the cone, the fourth region of the map.

The influence of the bulk cohesion ($C_B = 7$ MPa) on the shape of this grey cone is examined in Fig. 8(b). The cone with zero cohesion is also presented for the sake of comparison. The cone internal angle is larger in the presence of cohesion and the cone is shifted towards smaller values of the detachment effective friction coefficient. Note that the singular behaviour at the cone tip is regularized once cohesion is accounted for. Note also that cohesion enlarges the distance between the $\tilde{L}_{JG} \to \infty$ stability limit and our predictions. To illustrate these points, consider for example the friction coefficients $\mu'_B = 0.1, \mu'_D = 0.01$ signalled by the triangle symbol, corresponding to a central position within the cone for zero cohesion. The addition of cohesion renders this point stable. The central position in the cone with cohesion at $\mu'_B = 0.1$ would be $\mu'_D = 0.005$, half of the value in the absence of cohesion. It would be approximately a third of the value found on the $\tilde{L}_{JG} \to \infty$ curve for the same bulk friction coefficient.

The predicted stability limits are now examined in the (α, β) space, which was considered in section 4.1, to make a link with the work of Bilotti & Shaw (2005). Their ten cross-sections in terms of the couple (α, β) are shown as black squares in Fig. 9 and the white square marks the average value. The two graphs in the top row correspond to zero cohesion and the lower two are for a bulk cohesion of 7 MPa. The two graphs on the left column correspond to $\Delta\lambda_D = 0.55$ ($\mu'_D = 0.01$) and the two graphs on the right column to $\Delta\lambda_D = 0.57$ ($\mu'_D = 0.03$). The grey region corresponds to the grey cones discussed in Fig. 8(b) and the upper and the lower curves bounding each grey region correspond to the dimensionless lengths of 30 and 70, respectively, as judged from their relative positions with respect to the CCW solution ($\tilde{L}_{JG} \to \infty$).

The whole idea of this analysis is to figure out the range of fluid overpressures depending on the cohesion for which the average value of Bilotti & Shaw (2005) is within our grey regions. To illustrate the difference between Bilotti & Shaw's (2005) approach and our Limit Analysis, we have also plotted in the top left graph the CCW theory for the compressive wedge, disregarding cohesion (dashed curve) and accounting for cohesions (10 and 1 MPa for the bulk material and the detachment, respectively, dotted curve from Bilotti & Shaw 2005). The grey regions are bounded by curves which are increasing functions of the detachment dip. To the contrary, the dotted and dashed curves are decreasing functions of the same variable. This is simply a consequence of the fact that the two approaches do not correspond to the same boundary of the stability domain as presented in Fig. 5(b). The dotted and dashed curves correspond to the lower boundary whereas our predictions are shown by the generic dot-dashed curve which has a slope of same sign as the upper boundary (extensional) of the CCW theory.

Consider the cohesionless case, Figs 9(a) and (b) for $\Delta\lambda_D = 0.55$ and 0.57, respectively. In the left graph, the bulk overpressure ratio must be close to 0.5 (approximately 0.47) for the white square to be in the associated grey region. In the right graph, the white square is found in the grey region associated to $\Delta\lambda_B = 0.4$. Adding cohesion, Figs 9(c) and (d), increases the bulk overpressure ratio to 0.5 for the two detachment overpressure ratios. Note that cohesion has a more drastic influence on our stability predictions than on the purely compressive predictions (little difference between the dotted and dashed curves).

We now summarize the findings from Figs 8 and 9. An onset of gravity instability linking the three structural domains implies that $\mu'_D \leq 0.017$ and $\mu'_B \leq 0.27$, in the absence of cohesion (tip of grey cone and maximum μ'_B for the upper limit of the cone in Fig. 8a). The fluid overpressure ratio $\Delta\lambda_B$ is between 0.4 and 0.5, and $\Delta\lambda_D \geq 0.55$ (with a maximum value at 0.57), Figs 9(a) and (b). If the bulk material has a cohesion of 7 MPa, then the bounds are $\mu'_D \leq 0.02$ and $\mu'_B \leq 0.2$, Fig. 8(b). The fluid overpressure ratio $\Delta\lambda_B$ is likely to be 0.5 in the bulk and in the range 0.55–0.57 within the detachment, Figs 9(c) and (d).

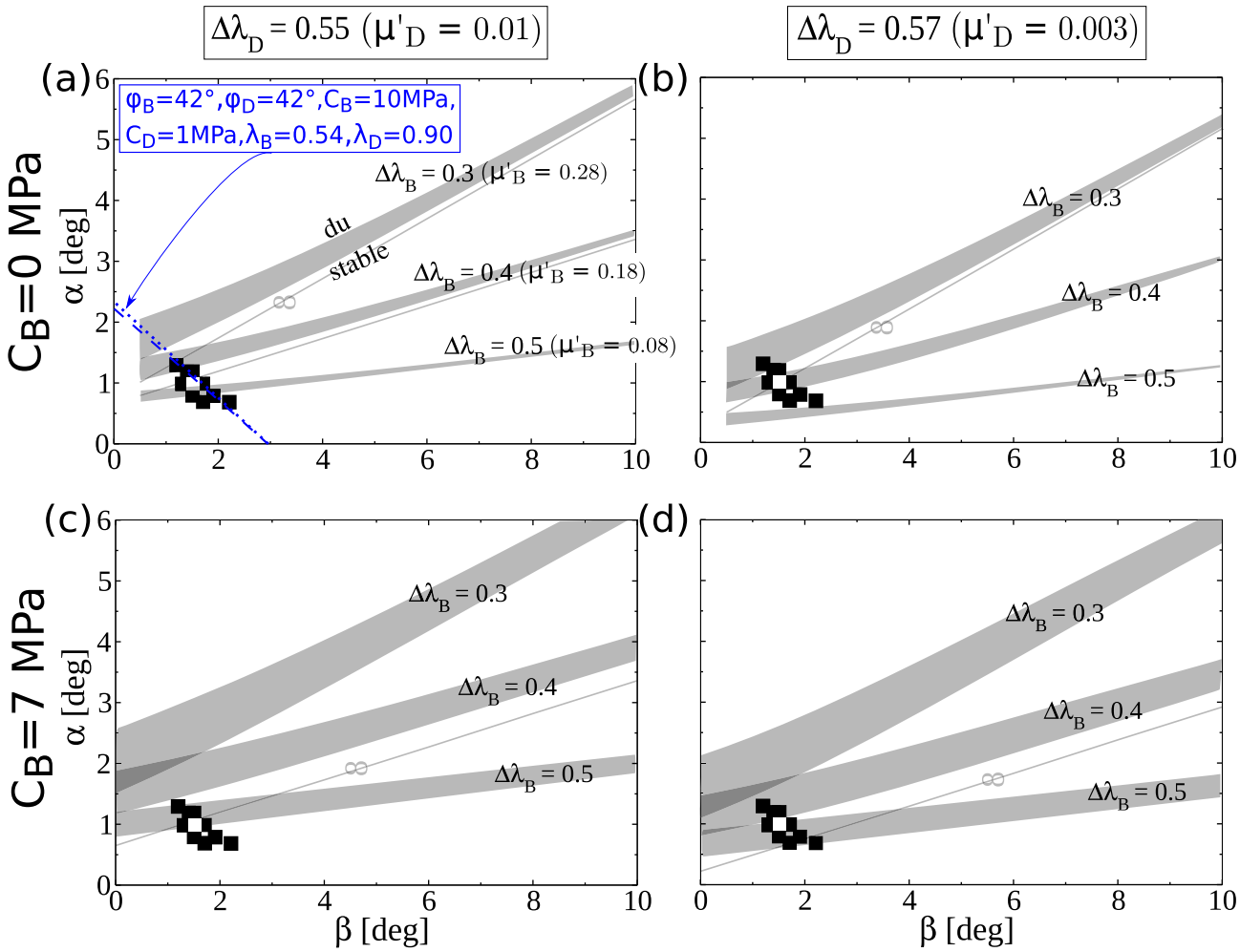

Figure 9. The stability predictions according to the Limit Analysis (setting friction angle $\varphi_D = 10^\circ$) and to Bilotti & Shaw (2005) for the Niger Delta in the space spanned by the critical surface slope and the detachment dip. The fluid overpressure ratio $\Delta\lambda_D$ is 0.55 and 0.57 in the left and the right column, respectively. The bulk cohesion C_B is 0 and 7 MPa in the top row and in the bottom row, respectively. The black squares and their average (the white square) are data from Bilotti & Shaw (2005). They are fitted by the dotted curve determined from the CCW theory assuming tectonic compressive collapse. The grey shaded domains present the uncertainty on the collapse length ($\tilde{L}_{JG} = 30-70$) and are predictions of the Limit Analysis accounting for interaction between the three domains of the collapsing wedge.

5 CONCLUDING DISCUSSION

This contribution proposes an application of Limit Analysis to the gravity instability of offshore deltas linking the upslope extensional half-graben (province B in Fig. 10a) to the downslope compressive thrusting (province A in same figure) with the sliding of the transitional domain. The methodology accounts for topographies of any shape and for pore pressure fields in frictional and cohesive materials.

It is shown, for a homogeneous inclined layer, that the onset of gravity instability always occurs for the longest possible detachment length by increasing the detachment overpressure. Cohesion requires a larger overpressure for the instability onset but does not change this longest length selection. It is proved that the fault dips are exactly predicted by the CCW theory if the collapse mechanism is composed of planar faults and axial surfaces. Such predictions for the normal fault dips are validated by matching the experimental results on normal faulting triggered by air overpressure in sand analogues (Mourgues & Cobbold 2003).

For offshore wedges, the relative positions of the upper and lower slope breaks, controlled partly by sedimentation processes, define the maximum available length for the instability. We demonstrate that the dimensionless length defined by the ratio of this active detachment length to the thickness of the sediments at the frontal toe controls the importance of the interaction between the three provinces of the delta. If that dimensionless length is greater than 100, simplified theories such as the CCW theory are sufficient to capture the stability conditions. Below this value, the interaction between the three provinces is crucial to obtain accurate predictions. For the example of the Niger Delta, the dimensionless length is in the range of 30–70. The fluid pressures are determined by considering the wedge of surface slope 1° and detachment dip 1.5° to be at the instability onset. For cohesionless materials, it is shown that the pore-fluid pressure within the bulk material is 80–90 per cent of the lithostatic pressure (Hubbert–Rubey fluid-pressure ratio $\lambda_B = 0.8$–0.9). For the detachment, the pressure is 97–99 per cent of the lithostatic pressure, slightly larger values than predicted by Albertz *et al.* (2010). Cohesion increases the bulk pressure ratio close to 0.9 but cannot change the detachment pressure predictions which are already at the maximum available range.

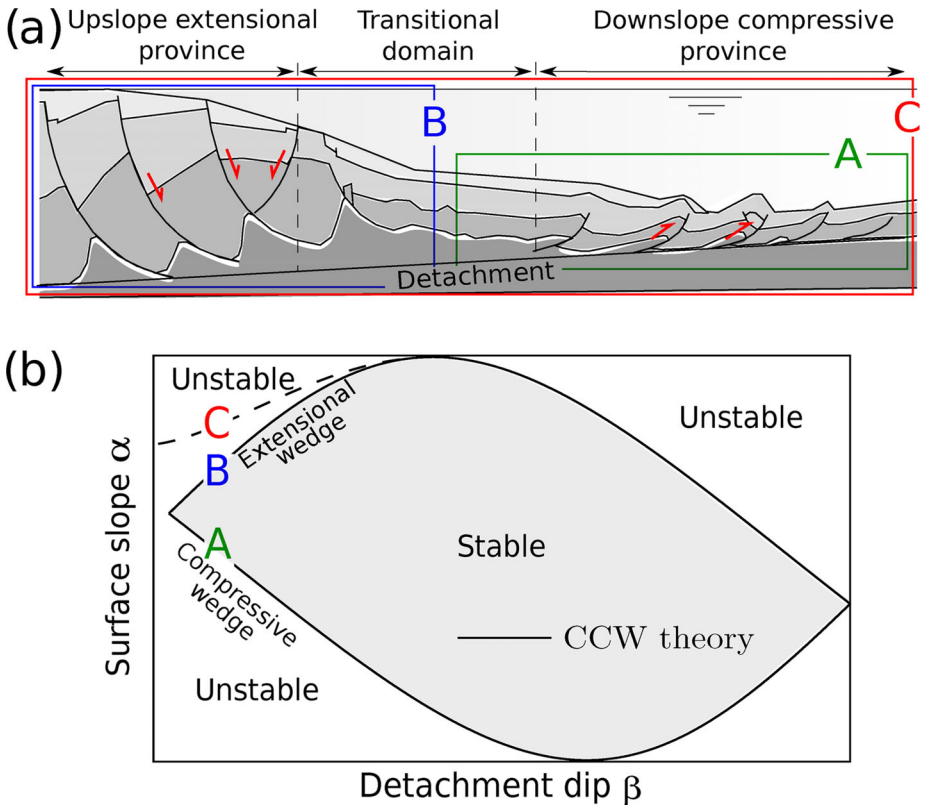

Figure 10. (a) Schematic illustration of upslope extensional (B), transitional and downslope compressive (A) provinces, composing the gravity-driven collapse of offshore deltas (modified from King *et al.* 2010). (b) The stability domain in the (α, β) plane according to the CCW theory (Dahlen 1984), accounting for either extension or compression, and the amendment due to the three province interaction (dashed curve C).

Information on the Niger Delta wedge geometry were based on the work of Bilotti & Shaw (2005) who focused on the compressive domain and applied the CCW theory. Their findings correspond to the curve A of the stability boundary presented in Fig. 10(b) whereas our predictions are associated to the dashed curve C on the same graph. The difference between their and our stability predictions in terms of detachment fluid overpressure are of the order of 10 per cent which is marginal in view of the data accuracy. This small difference in overpressure is surprising because of the small dimensionless active transitional length whose importance was discussed above. We believe that the account of bulk cohesion cannot justify this lack of difference. The reason for it is more likely due to the selection of the friction angle because Bilotti & Shaw (2005) chose $\varphi_B = \varphi_D = 42^\circ$. Lower values (for example $\varphi_B = 30^\circ$, $\varphi_D = 10^\circ$, more consistent with our selection) would lead to the very different prediction of $\lambda_D = 0.49$ with the CCW theory, which is only 49 per cent of the lithostatic pressure. It is only by having similar friction angles that the difference in stability predictions between the CCW theory and the Limit Analysis can be revealed.

This contribution is a first tentative in linking the three provinces of a collapsing delta using Limit Analysis and could be complemented in the future by different actions. Three aspects are now discussed. First, the geometry of the detachment is most likely not planar (Corredor *et al.* 2005) and the introduction of a segmented detachment, corresponding to change in activation depth, is certainly possible and of interest. Second, it is most likely that the shale compaction is not uniform along the 200 km long detachment and should be described by varying the pressure ratio as considered by Pons *et al.* (2013) for the application to Nankai wedge, Japan. Third and more important, the present contribution is the first building block required to develop the sequential version of Limit Analysis (Cubas *et al.* 2008; Mary *et al.* 2013a,b) which aims at following the evolution of the wedge in time. Two steps are solved at each increment. The first step corresponds to the prediction of the dominant collapse mechanism as it was done in this contribution and the second step consists in a modification of the geometry according to simple geometric rules inspired from the half-graben kinematics (Groshong 1989; Xiao & Suppe 1992) and the classical fault-bend fold (Suppe 1983). This structural evolution could also account for slip weakening once the faults slide, prograding depositional processes and variation of the detachment pressures in time.

ACKNOWLEDGEMENTS

XPY benefited from the support of the China Scholarship Council during his doctoral studies in France. The authors thank professors Carole Petit, Michele Cooke and the Editor Bert Vermeersen for their comments which contributed to substantially improve the final version of this manuscript.

REFERENCES

Albertz, M., Beaumont, C. & Ings, S.J., 2010. Geodynamic modeling of sedimentation-induced overpressure, gravitational spreading, and deformation of passive margin mobile shale basins, *AAPG Memoir,* **93,** 29–62.

Bilotti, F. & Shaw, J.H., 2005. Deep-water Niger Delta fold and thrust belt modeled as a critical-taper wedge: the influence of elevated basal fluid pressure on structural styles, *AAPG Bull.,* **89**(11), 1475–1491.

Bonnelye, A., Schubnel, A., David, C., Henry, P., Guglielmi, Y., Gout, C., Fauchille, A. & Dick, P., 2016. Strength anisotropy of shales deformed under uppermost-crustal conditions, *J. geophys. Res.,* **121,** doi:10.1002/2016JB013040.

Butler, R., 2010. Stratigraphic correlations across the Niger Delta, http://www.seismicatlas.org/.

Byerlee, J., 1978. Friction of rocks, *Pure appl. Geophys.,* **116**(4–5), 615–626.

Chen, W., 1975. *Limit Analysis and Soil Plasticity,* Elsevier.

Cobbold, P., Mourgues, R. & Boyd, K., 2004. Mechanism of thin-skinned detachment in the Amazon Fan: assessing the importance of fluid overpressure and hydrocarbon generation, *Mar. Pet. Geol.,* **21**(8), 1013–1025.

Corredor, F., Shaw, J. & Bilotti, F., 2005. Structural styles in the deep-water fold and thrust belts of the Niger Delta, *AAPG Bull.,* **89**(6), 753–780.

Crans, W., Mandl, G. & Haremboure, J., 1980. On the theory of growth faulting: a geomechanical delta model based on gravity sliding, *J. Pet. Geol.,* **2**(3), 265–307.

Cubas, N., Leroy, Y.M. & Maillot, B., 2008. Prediction of thrusting sequences in accretionary wedges, *J. geophys. Res.,* **113,** B12412, doi:10.1029/2008JB005717.

Dahlen, F.A., 1984. Noncohesive critical Coulomb wedges: an exact solution, *J. geophys. Res.,* **89**(B12), 10 125–10 133.

Damuth, J.E., 1994. Neogene gravity tectonics and depositional processes on the deep Niger Delta continental margin, *Mar. Pet. Geol.,* **11**(3), 320–346.

Ge, H., Jackson, M.P. & Vendeville, B.C., 1997. Kinematics and dynamics of salt tectonics driven by progradation, *AAPG Bull.,* **81**(3), 398–423.

Groshong, R.H., 1989. Half-graben structures: balanced models of extensional fault-bend folds, *Bull. geol. Soc. Am.,* **101**(1), 96–105.

Hooper, R., Fitzsimmon, R., Grant, N. & Vendeville, B., 2002. The role of deformation in controlling depositional patterns in the south-central Niger Delta, West Africa, *J. Struct. Geol.,* **24**(4), 847–859.

Hubbert, M.K. & Rubey, W.W., 1959. Role of fluid pressure in mechanics of overthrust faulting: I. Mechanics of fluid-filled solids and its application to overthrust faulting, *Bull. geol. Soc. Am.,* **70,** 115–166.

King, R.C., Tingay, M.R., Hillis, R.R., Morley, C.K. & Clark, J., 2010. Present-day stress orientations and tectonic provinces of the NW Borneo collisional margin, *J. geophys. Res.,* **115,** B10415, doi:10.1029/2009JB006997.

Kohli, A.H. & Zoback, M.D., 2013. Frictional properties of shale reservoir rocks, *J. geophys. Res.,* **118**(9), 5109–5125.

Krueger, S.W. & Grant, N.T., 2011. The growth history of toe thrusts of the Niger Delta and the role of pore pressure, *AAPG Memoir,* **94,** 357–390.

Lacoste, A., Vendeville, B.C., Mourgues, R., Loncke, L. & Lebacq, M., 2012. Gravitational instabilities triggered by fluid overpressure and downslope incision - insights from analytical and analogue modelling, *J. Struct. Geol.,* **42,** 151–162.

Leduc, A.M., Davies, R.J., Densmore, A.L. & Imber, J., 2012. The lateral strike-slip domain in gravitational detachment delta systems: a case study of the northwestern margin of the Niger Delta, *AAPG* Bull., **96**(4), 709–728.

Lehner, F.K., 1986. Noncohesive critical Coulomb wedges: an exact solution—Comments, *J. geophys. Res.,* **91**(B1), 793–796.

Maillot, B. & Leroy, Y.M., 2006. Kink-fold onset and development based on the maximum strength theorem, *J. Mech. Phys. Solids,* **54**(10), 2030–2059.

Maloney, D., Davies, R., Imber, J., Higgins, S. & King, S., 2010. New insights into deformation mechanisms in the gravitationally driven Niger Delta deep-water fold and thrust belt, *AAPG Bull.,* **94**(9), 1401–1424.

Mary, B., Maillot, B. & Leroy, Y.M., 2013a. Deterministic chaos in frictional wedges revealed by convergence analysis, *Int. J. Numer. Anal. Methods Geomech.,* **37,** 3036–3051.

Mary, B., Maillot, B. & Leroy, Y.M., 2013b. Predicting orogenic wedge styles as a function of analogue erosion law and material softening, *Geochem. Geophys. Geosyst.,* **14,** 4523–4543.

McClay, K., Dooley, T. & Lewis, G., 1998. Analog modeling of progradational delta systems, *Geology,* **26**(9), 771–774.

Morgan, R., 2006. The Niger delta: an active passive margin, *GEO Expro,* **4**(5), 36.

Mourgues, R. & Cobbold, P., 2003. Some tectonic consequences of fluid overpressures and seepage forces as demonstrated by sandbox modelling, *Tectonophysics,* **376,** 75–97.

Mourgues, R. & Cobbold, P., 2006a. Thrust wedges and fluid overpressures: Sandbox models involving pore fluids, *J. geophys. Res.,* **111,** B05404, doi:10.1029/2004JB003441.

Mourgues, R. & Cobbold, P.R., 2006b. Sandbox experiments on gravitational spreading and gliding in the presence of fluid overpressures, *J. Struct. Geol.,* **28**(5), 887–901.

Mourgues, R., Lecomte, E., Vendeville, B. & Raillard, S., 2009. An experimental investigation of gravity-driven shale tectonics in progradational delta, *Tectonophysics,* **474**(3–4), 643–656.

Mourgues, R., Lacoste, A. & Garibaldi, C., 2014. The Coulomb critical taper theory applied to gravitational instabilities, *J. geophys. Res.,* **119**(1), 754–765.

Pons, A. & Leroy, Y.M., 2012. Stability of accretionary wedges based on the maximum strength theorem for fluid-saturated porous media, *J. Mech. Phys. Solids,* **60,** 643–664.

Pons, A. & Mourgues, R., 2012. Deformation and stability of over-pressured wedges: insight from sandbox models, *J. geophys. Res.,* **117,** B09404, doi:10.1029/2012JB009379.

Pons, A., Leroy, Y.M. & Lallemant, S., 2013. Fluid pressure control on splay fault activation in accretionary prism based on the maximum strength theorem with application to the Nankai wedge, *Earth planet. Sci. Lett.,* **368,** 43–50.

Rowan, M.G., Peel, F.J. & Vendeville, B.C., 2004. Gravity-driven fold belts on passive margins, *AAPG Memoir,* **82,** 157–182.

Salençon, J., 2002. *De l'élasto-plasticité au calcul à la rupture,* École Polytechnique, Palaiseau, and Ellipses.

Silva, S., Maciel, R. & Severino, M., 1998. Cenozoic tectonics of Amazon Mouth basin, *Geo-Marine Lett.,* **18**(3), 256–262.

Suppe, J., 1983. Geometry and kinematics of fault-bend folding, *Am. J. Sci.,* **283,** 684–721.

Suppe, J., 2007. Absolute fault and crustal strength from wedge tapers, *Geology,* **35**(12), 1127–1130.

Suppe, J., 2014. Fluid overpressures and strength of the sedimentary upper crust, *J. Struct. Geol.,* **69**(Part B), 481–492.

Tingay, M.R., Hillis, R.R., Swarbrick, R.E., Morley, C.K. & Damit, A.R., 2009. Origin of overpressure and pore-pressure prediction in the Baram province, Brunei, *AAPG Bull.,* **93**(1), 51–74.

Vendeville, B.C., 2005. Salt tectonics driven by sediment progradation: Part I. Mechanics and kinematics, *AAPG Bull.,* **89**(8), 1071–1079.

Wang, K., He, J. & Hu, Y., 2006. A note on pore fluid pressure ratios in the Coulomb wedge theory, *Geophys. Res. Lett.,* **33,** L19310, doi:10.1029/2006GL027233.

Weber, K. & Daukoru, E., 1975. Petroleum geology of the Niger Delta, in *9th World Petroleum Congress Proceedings,* Tokyo, Japan, vol. 2, pp. 209–221.

Wu, S. & Bally, A.W., 2000. *Slope Tectonics-Comparisons and Contrasts of Structural Styles of Salt and Shale Tectonics of the Northern Gulf of Mexico with Shale Tectonics of Offshore Nigeria in Gulf of Guinea,* pp. 151–172, American Geophysical Union.

Xiao, H.-B. & Suppe, J., 1992. Orgin of rollover, *AAPG Bull.,* **76**(4), 509–529.

Yuan, X.P., Leroy, Y.M. & Maillot, B., 2015. Tectonic and gravity extensional collapses in overpressured cohesive and frictional wedges, *J. geophys. Res.,* **120**(3), 1833–1854.

SUPPORTING INFORMATION

Supplementary data are available at *GJIRAS* online.

Figure ES1. (a) The definition of the fluid pressure ratio is function of distance from the point of interest within the wedge to the topographic surface. The black segment was proposed by Hubbert & Rubey (1959) and blue segment was considered by Lacoste *et al.* (2012). (b) The illustration of the definition for fluid pressure ratio $\lambda^{(H)}$ and overpressure ratio $\Delta\lambda^{(H)}$ in Hubbert & Rubey (1959).

Please note: Oxford University Press is not responsible for the content or functionality of any supporting materials supplied by the authors. Any queries (other than missing material) should be directed to the corresponding author for the paper.

APPENDIX A: DETAILS OF LIMIT ANALYSIS SOLUTIONS

The first objective of this appendix is to provide the effective external power and the maximum resisting power in eqs (5) and (6), respectively. The second objective is to specialize these expressions for the cases of the inclined layer and of the wedge prototype.

A1 General solution

The velocity field is piecewise-uniform over the prototype and is selected such that the velocity jumps are not parallel to the discontinuity but at a corresponding friction angle, as presented in Fig. A1 for the upslope and the downslope parts of the collapse mechanism. The norms of velocity jumps are then determined from the hodographs presented on the same figure and the normalization is with respect to the sliding block velocity.

The effective external power $\mathcal{P}'_{\text{ext}}(\hat{\underline{U}})$ in eq. (5) for this velocity field is

$$\begin{aligned}\mathcal{P}'_{\text{ext}}(\hat{\underline{U}}) = {} & \rho \underline{g} \cdot (S_{\text{HG}}\hat{\underline{U}}_{\text{HG}} + S_{\text{SB}}\hat{\underline{U}}_{\text{SB}} + S_{\text{HW}}\hat{\underline{U}}_{\text{HW}}) \\ & + \int_J^H p_{JH}\,\mathrm{d}S\,\underline{n}_{JH}\cdot\hat{\underline{U}}_{\text{HG}} + \int_J^I p_{JI}\,\mathrm{d}S\,\underline{n}_{JI}\cdot\hat{\underline{J}}_{JI} + \int_G^F p_{GF}\,\mathrm{d}S\,\underline{n}_{GF}\cdot\hat{\underline{J}}_{GF} \\ & + \int_G^E p_{GE}\,\mathrm{d}S\,\underline{n}_{GE}\cdot\hat{\underline{U}}_{\text{HW}} + \int_J^G p_D\,\mathrm{d}S\,\underline{n}_{JG}\cdot\hat{\underline{U}}_{\text{SB}} \\ & + \int_H^I p_f\,\mathrm{d}S\,\underline{n}_{HI}\cdot\hat{\underline{U}}_{\text{HG}} + \int_E^F p_f\,\mathrm{d}S\,\underline{n}_{EF}\cdot\hat{\underline{U}}_{\text{HW}} + \int_F^I p_f\,\mathrm{d}S\,\underline{n}_{FI}\cdot\hat{\underline{U}}_{\text{SB}}\,. \end{aligned} \tag{A1}$$

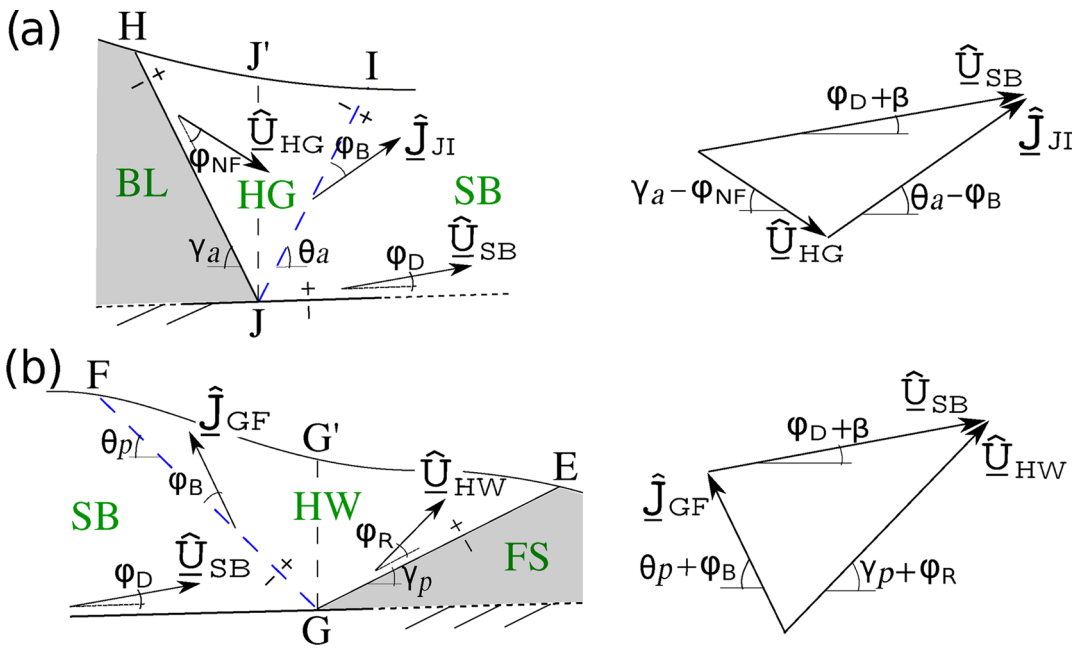

Figure A1. The velocity field for the extensional and the compressive parts of the collapse mechanism in (a) and (b), respectively, with the associated hodographs of the velocity jumps across the axial surfaces *JI* and *GF*.

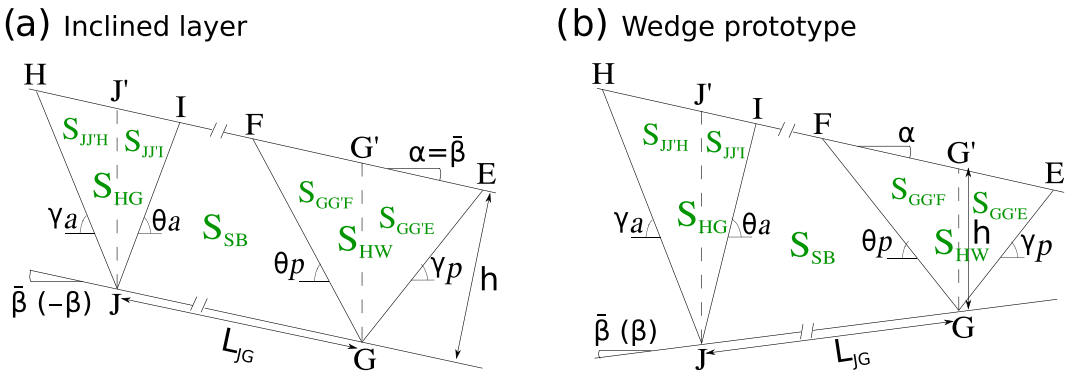

Figure A2. Geometries of (a) Inclined layer and (b) wedge prototype used to calculate the block sizes.

The first term in the right-hand side of eq. (A1) corresponds to the power of the velocity field on the gravity in the HG, the SB and the HW. The next five integrals are the contributions of the power of the velocity jumps on the fluid pressure within the normal fault *JH*, the upslope axial surface *JI*, the downslope axial surface *GF*, the thrust ramp *GE*, and the detachment *JG*. Note that p_{XY} denotes the fluid pressure between point *X* and *Y* and $\underline{n}_{XY}$ indicates the normal vector to segment *XY*. The last three terms in (A1) result from the power of the fluid pressure on the topography.

Expression (A1) is now simplified by application of the following weak form of Archimedes' theorem as explained in the Electronic Supplement of paper 1: the power of the velocity field on the hydrostatic part of the pressure is equal to the opposite of the power of the same velocity field on the vertical forces resulting from the weight of the displaced regions, if assumed composed of a material of volumetric mass ρ_f. The effective external power (A1) is then expressed simply in terms of the departure from the hydrostatic pressure as

$$\begin{aligned}\mathcal{P}'_{\rm ext}(\hat{\underline{U}}) = {} & (\rho-\rho_f)\underline{g}\cdot\left(S_{\rm HG}\hat{\underline{U}}_{\rm HG}+S_{\rm SB}\hat{\underline{U}}_{\rm SB}+S_{\rm HW}\hat{\underline{U}}_{\rm HW}\right)\\ & +\int_J^H \Delta p_{JH}\,{\rm d}S\,\underline{n}_{JH}\cdot\hat{\underline{U}}_{\rm HG}+\int_J^I \Delta p_{JI}\,{\rm d}S\,\underline{n}_{JI}\cdot\hat{\underline{J}}_{JI}+\int_G^F \Delta p_{GF}\,{\rm d}S\,\underline{n}_{GF}\cdot\hat{\underline{J}}_{GF}\\ & +\int_G^E \Delta p_{GE}\,{\rm d}S\,\underline{n}_{GE}\cdot\hat{\underline{U}}_{\rm HW}+\int_J^G \Delta p_D\,{\rm d}S\,\underline{n}_{JG}\cdot\hat{\underline{U}}_{\rm SB}\,.\end{aligned} \tag{A2}$$

Two operations are now conducted. First, the orientation of the velocity field is explicitly accounted for and second, the pressures are expressed in terms of the overpressure ratios in eq. (1) so that the integrals in eq. (A2) are estimated exactly. For that purpose, the points *J*′ and *G*′ are introduced on the topography to have the same x_1-coordinate as points *J* and *G*, respectively, Fig. A1. The effective external power in eq. (A2) then becomes:

$$\begin{aligned}\mathcal{P}'_{\rm ext}(\hat{\underline{U}}) = {} & (\rho-\rho_f)g\left[S_{\rm HG}\hat{U}_{\rm HG}\sin(\gamma_a-\varphi_{NF})-S_{\rm SB}\hat{U}_{\rm SB}\sin(\beta+\varphi_D)-S_{\rm HW}\hat{U}_{\rm HW}\sin(\gamma_p+\varphi_R)\right]\\ & +\rho g\Big[\Delta\lambda_{NF}\,S_{JJ'H}\hat{U}_{\rm HG}\frac{\sin(\varphi_{NF})}{\cos(\gamma_a)}+\Delta\lambda_B\,S_{JJ'I}\hat{J}_{JI}\frac{\sin(\varphi_B)}{\cos(\theta_a)}+\Delta\lambda_B\,S_{GG'F}\hat{J}_{GF}\frac{\sin(\varphi_B)}{\cos(\theta_p)}\\ & +\Delta\lambda_R\,S_{GG'E}\hat{U}_{\rm HW}\frac{\sin(\varphi_R)}{\cos(\gamma_p)}+\Delta\lambda_D\,S_{JJ'G'G}\hat{U}_{\rm SB}\frac{\sin(\varphi_D)}{\cos\beta}\Big],\end{aligned} \tag{A3}$$

in which, S_{XYZ} is the area of the surface having the apexes *X*, *Y* and *Z*.

The maximum resisting power defined in eq. (6) for this velocity field is

$$\begin{aligned}\mathcal{P}'_{\rm mr}(\hat{\underline{U}}) = {} & C_D L_{JG}\cos(\varphi_D)\hat{U}_{\rm SB}+C_{NF}L_{JH}\cos(\varphi_{NF})\hat{U}_{\rm HG}+C_B L_{JI}\cos(\varphi_B)\hat{J}_{JI}\\ & +C_R L_{GE}\cos(\varphi_R)\hat{U}_{HW}+C_B L_{GF}\cos(\varphi_B)\hat{J}_{GF}\,,\end{aligned} \tag{A4}$$

which corresponds to the sum of the maximum resisting power over the discontinuities *JG*, *JH*, *JI*, *GE* and *GF*, respectively.

A2 Inclined layer

For the inclined layer in Fig. A2(a), the lengths found in eq. (A4) are

$$L_{JH}=h/\sin(\gamma_a+\beta)\,,\quad L_{JI}=h/\sin(\theta_a-\beta)\,,\quad L_{GE}=h/\sin(\gamma_p-\beta)\,,\quad L_{GF}=h/\sin(\theta_p+\beta)\,. \tag{A5}$$

The areas introduced in eq. (A3) are

$$S_{\rm HG} = h^2\big[\cot(\gamma_a+\beta)+\cot(\theta_a-\beta)\big]/2\,, \quad S_{\rm SB} = L_{JG}\,h - h^2\big[\cot(\theta_a-\beta)+\cot(\theta_p+\beta)\big]/2,$$

$$S_{\rm HW} = h^2\big[\cot(\theta_p+\beta)+\cot(\gamma_p-\beta)\big]/2\,, \quad S_{JJ'H} = \frac{h^2\cos(\gamma_a)}{2\,\sin(\gamma_a+\beta)\cos\beta}\,, \quad S_{JJ'I} = \frac{h^2\cos(\theta_a)}{2\,\sin(\theta_a-\beta)\cos\beta}\,,$$

$$S_{GG'E} = \frac{h^2\cos(\gamma_p)}{2\,\sin(\gamma_p-\beta)\cos\beta}\,, \quad S_{GG'F} = \frac{h^2\cos(\theta_p)}{2\,\sin(\theta_p+\beta)\cos\beta}\,, \quad S_{JJ'G'G} = L_{JG}\,h. \tag{A6}$$

Combining eq. (A3) with eqs (A5) and (A6) results in the effective external power in eq. (8) which is normalized by $\rho g h^2 \hat{U}_{BS}$.

A3 Wedge prototype

For the wedge prototype, the reference length is $L_{GG'} = h$, Fig. A2(b). The lengths required in eq. (A4) for the maximum resisting power are

$$L_{JH} = \frac{L_{JJ'}\cos\alpha}{\sin(\gamma_a-\alpha)}\,, \quad L_{JI} = \frac{L_{JJ'}\cos\alpha}{\sin(\theta_a+\alpha)}\,, \quad L_{GE} = \frac{h\cos\alpha}{\sin(\gamma_p+\alpha)}\,, \quad L_{GF} = \frac{h\cos\alpha}{\sin(\theta_p-\alpha)}\,,$$
$$\text{with} \quad L_{JJ'} = L_{JG}\sin\beta + h + L_{JG}\cos\beta\,\tan\alpha\,, \tag{A7}$$

and the areas found in eq. (A3) correspond to

$$S_{JJ'H} = \frac{L_{JJ'}^2\cos(\gamma_a)\cos\alpha}{2\,\sin(\gamma_a-\alpha)}\,, \quad S_{JJ'I} = \frac{L_{JJ'}^2\cos(\theta_a)\cos\alpha}{2\,\sin(\theta_a+\alpha)}\,, \quad S_{GG'E} = \frac{h^2\cos(\gamma_p)\cos\alpha}{2\,\sin(\gamma_p+\alpha)}\,,$$

$$S_{GG'F} = \frac{h^2\cos(\theta_p)\cos\alpha}{2\,\sin(\theta_p-\alpha)}\,, \quad S_{JJ'G'G} = \frac{(h+L_{JJ'})L_{JG}\cos\beta}{2}\,,$$

$$S_{\rm HG} = S_{JJ'H} + S_{JJ'I}\,, \quad S_{\rm HW} = S_{GG'E} + S_{GG'F}\,, \quad S_{\rm SB} = S_{JJ'G'G} - S_{JJ'I} - S_{GG'F}. \tag{A8}$$

The expressions in eqs (14) and (15) are obtained by combining eqs (A7) and (A8) with eqs (A3) and (A4).